DOI:10.16555/j.1006-8775.2014.02.010

Article ID: 1006-8775(2014) 02-0181-12

THE INFLUENCE OF CLOUD PARAMETERIZATION ADJUSTMENT USING REFLECTIVITY OF DOPPLER ON NOWCASTING WITH GRAPES MODEL

ZHANG Yan-xia (张艳霞), CHEN Zi-tong (陈子通), MENG Wei-guang (蒙伟光), HUANG Yan-yan (黄燕燕), DAI Guang-feng (戴光丰), DING Wei-yu (丁伟钰)

(Guangzhou Institute of Tropical and Marine Meteorology/Guangdong Provincial Key Laboratory of Regional Numerical Weather Prediction, China Meteorological Administration, Guangzhou 510080 China)

Abstract: In this study, we attempted to improve the nowcasting of GRAPES model by adjusting the model initial field through modifying the cloud water, rain water and vapor as well as revising vapor-following rain water. The results show that the model nowcasting is improved when only the cloud water and rain water are adjusted or all of the cloud water, rain water and vapor are adjusted in the initial field. The forecasting of the former (latter) approach during 0-3 (0-6) hours is significantly improved. Furthermore, for the forecast for 0-3 hours, the latter approach is better than the former. Compared with the forecasting results for which the vapor of the model initial field is adjusted by the background vapor with those by the revised vapor, the nowcasting of the revised vapor is much better than that of background vapor. Analysis of the reasons indicated that when the vapor is adjusted in the model initial field, especially when the saturated vapor is considered, the forecasting of the vapor field is significantly affected. The changed vapor field influences the circulation, which in turn improves the model forecasting of radar reflectivity and rainfall.

Key words: radar reflectivity; cloud parameter; vapor; precipitation; nudging; nowcasting

CLC number: P435 **Document code:** A

1 INTRODUCTION

In recent years, short-term forecast of mesoscale weather is conducted by increasing numerical forecasting models, but the initial fields of models mainly depend on background field and conventional sounding data given by large-scale atmospheric models. Spatial resolution with several hundred kilometers of background fields and sparse meteorological observation stations could not very well response to meso-characteristics of weather systems and much less so in distinguishing cloud-scale weather systems, making model forecasting hard to improve. The key of solving the problem lies in gaining high spatial and temporal resolution data to output the initial fields of meso-scale numerical models. There exist high spatial and temporal resolutions in Doppler data and the horizontal and vertical resolutions of their detecting radar reflectivity are about one kilometer. With Doppler, not only most meso- and small-scale weather systems are captured in the range of observation, but also the information of the vapor content of precipitation particles is well provided through its data. The objective forecasting of a meso-scale model will be improved if high resolution data are applied to the model. Now, various methods have been developed of using Doppler radar data to retrieve atmospheric three-dimensional wind and temperature fields[1-5], improving the initial fields of meso-scale atmospheric models, and thereby increasing the accuracy rates of numerical nowcasting and short-term weather forecasting[6-8].

Cloud parameters are those of important elements describing the atmospheric state on the cumulus scale. Now, for most meso-scale atmospheric models, such as ARPS, MM5, GRAPES, cloud parameters of model grid-scale are required to be present in the initial field. However, the initial physical elements are set to zero because of the scarce observation data. There exist cloud micro-physical elements in the model only after

Received 2013-01-31; **Revised** 2013-10-29; **Accepted** 2014-04-15

Foundation item: National Natural Science Foundation of China (41075083); On the Techniques of 0-6h Quantitative Forecast of Rain (Snow) (GYHY201006001); Science and Technology Planning Project for Guangdong Province (2011A032100006, 2012A061400012)

Biography: ZHANG Yan-xia, Ph.D., primarily undertaking research on numerical weather forecasting and tropical weather.

Corresponding author: ZHANG Yan-xia, e-mail: yxzhang@grmc.gov.cn

the model atmosphere is adjusted and the model generates the cloud. The drawback shows that there is observed precipitation in the initial time of model integrating while no precipitation is predicted in the model during a period of integration or there exist obvious differences in precipitation intensity and location between the model forecast and observation. Ascending motion corresponding to the convergence of initial field could not be supported by the release of latent heat of condensation if there is no sufficient vapor water in the initial field[9]. Therefore, the observed high-resolution water vapor field is introduced to the initial field, which directly modifies the moisture of initial field in the model.

In recent years, a lot of studies used the radar reflectivity data to modify the initial field of meso-scale numerical models. For example, the vertical velocity, vapor and cloud water are adjusted according to the semi-empirical relationship between the radar reflectivity intensity and the precipitation rate, which could effectively relieve the spin-up phenomena and improve the precipitation forecast[10-11]. The humidity adjustment can significantly improve the precipitation forecast by using radar reflectivity intensity data to carry out cloud analysis and diabatic initialization (Zhang[12]). The radar data can improve the location and intensity of precipitation through experiments with the MM5 model and the dynamic and thermodynamic diabatic initialization of the model are adjusted by retrieving radar precipitation data (Tuo et al.[13]). Radar data are assimilated into the model by using the Newton relaxation method and latent forcing, meanwhile, the role of increasing the humidity field in improving the forecast is further emphasized by Wang and Warner[14]. In a regional numerical model for rainstorms, radar data are applied and the results show that the humidity in the initial field is changed following the radar reflectivity intensity so that at the middle- and low-level vapor and converging upward motion increase in the rainstorm area as well as in the adjacent area, which makes the rainfall location and amount close to the observation[15]. Reasonable structures of meso- and fine-scale divergence and convergence are known by using radar reflectivity data to adjust atmospheric cloud microphysics in a 1-h nowcasting rainfall experiment[16].

Based on the results, good adjustment of cloud microphysics and humidity fields can improve the nowcasting of mesoscale models and play a significant role in the 0- to 6-h nowcasting. For this purpose, cloud microphysics and humidity field in the atmospheric initial field of a mesoscale model are adjusted in this work, through a numerical model experiment with strong precipitation occurring in South China and the nudging method with radar reflectivity, to improve the nowcasting.

This paper is organized as follows. Section 2 describes the datasets and methods used. Section 3 presents detailed analysis of the numerical experiment results and the concluding discussion is provided in section 4.

2 DATA, OBSERVATION AND METHOD

A heavy rainfall process happening on 14–15 May in 2010 is chosen in this paper. At 08:00 on 14 May (Beijing Time, same below), a main rainband occurred from southern Jiangxi to northern Guangdong and middle Guangxi and hourly rainfall amount reached 58.4 mm. The rainband slightly moved toward the south and stayed in northern Guangdong and Guangxi at 09:00–13:00 when the maximum hourly rainfall amount reached 77.7 mm. From 14:00, the center of heavy rainfall moved toward the middle of Guangdong and the maximum hourly rainfall amount at Qingyuan station achieved 83.8 mm at 16:00. The rainfall centre sequentially moved to the Pearl River Delta area and the rainfall amount by two automatic weather stations located in Guangzhou was as much as 79.9 mm (G1040) at 18:00 and 92.6 mm at 19:00 (G1006). The rainfall amount changed to 69.9 mm and 69.3 mm at 20:00 and 21:00, respectively. The precipitation decreased after 21:00 and the hourly rainfall amount was over 70 mm before dawn on 15 May. Meanwhile, a local rainstorm happened in Yangjiang and the rainfall amount was 92.4 mm. The 0-6 h nowcasting of the model is considered in the paper, therefore, the observed rainfall during 09:00–14:00 on 14 May is given (Fig. 1a). In addition, the center and movement of the rainband are shown from the observed hourly radar reflectivity.

Nine elevations of radar reflectivity from fourteen radars in Southern China at 08:00 on 14 May are used in the numerical model in this paper. The background field, which is used to calculate cloud water (*qc*, unit: g/kg) and rain water (*qr*, unit: g/kg) is the analytical field of GRAPES model with a resolution of 12 km. By using a simple cloud scheme in Brewster[17], only *qc* and *qr* in many cloud microphysical elements are retrieved. The pressure (*p*) and temperature (*T*) are gained from the analytical field of GRAPES model with a resolution of 12 km. The atmospheric density is calculated with *p* and *T* and *qr* is used with the radar reflectivity factor (dBz). The relationship between *qr* and radar reflectivity is expressed as follows.

$$qr = 10.0^{((\mathrm{dBz}-43.1)/17.5)} / \rho$$

In the expression, the calculated radar reflectivity lies between 15 dBz and 55 dBz. If the value is less than 15 dBz, it indicates there is no precipitation. If the value is greater than 55 dBz, it indicates precipitation in solid type. ρ is the atmospheric density and the function of pressure and temperature.

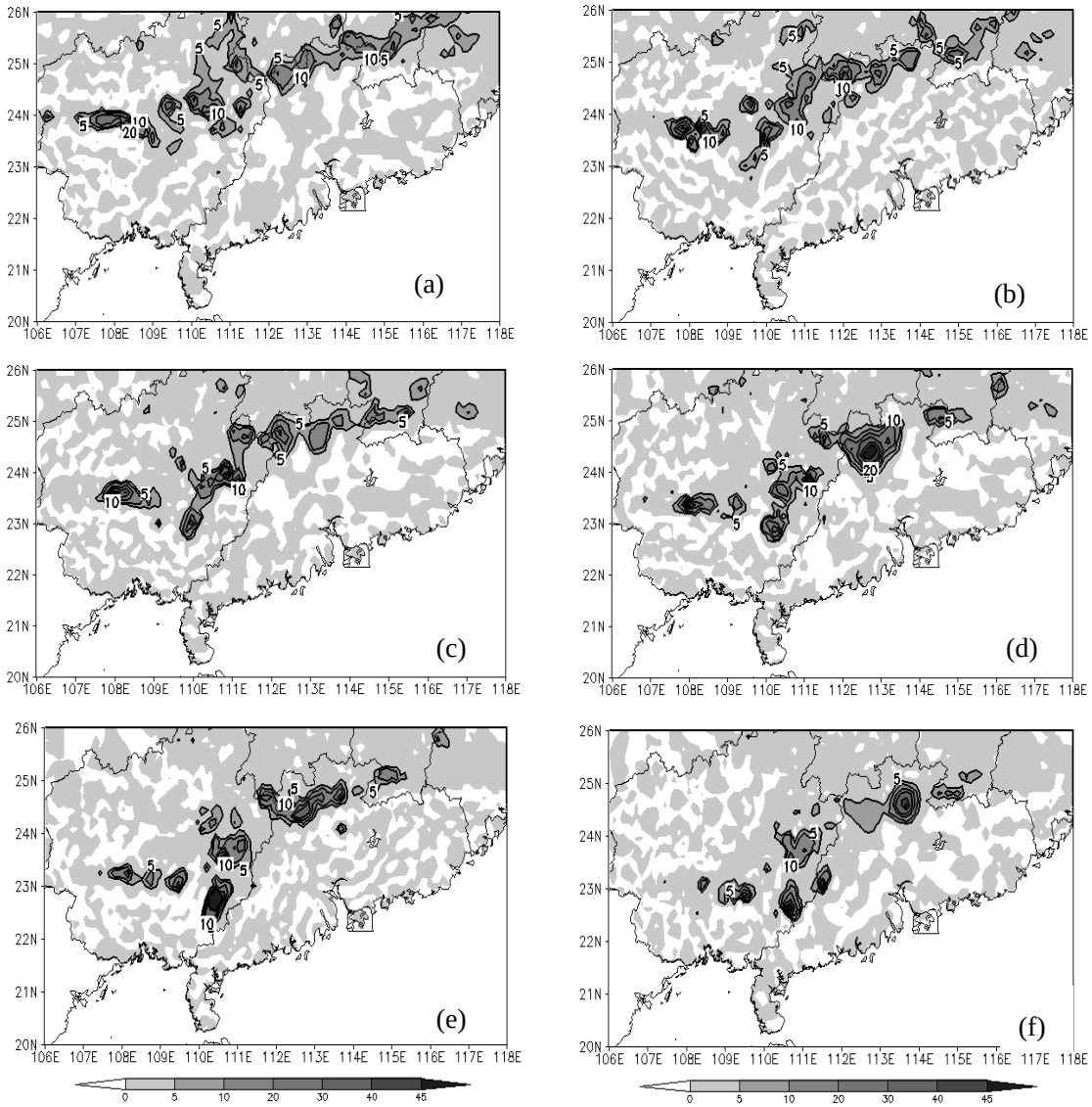

Figure 1. Distributions of 1-h observed rainfall on May 14 at 08:00 (a), 09:00 (b), 10:00 (c), 11:00 (d), 12:00 (e), and 13:00 (f).

The cloud water (*qc*) is the function of rain water, dropping speed and atmospheric density, namely, *qc* is the indirect function of radar reflectivity. The formula is as follows.

$vt=5.40\times(ps / p)^{0.4}\times QR^{0.125}$, where *ps* is the surface pressure, *p* the pressure at every level, *Qr* the rain water and *vt* the dropping speed.

$ir=(qr1\times vt1\times\rho1-qr2\times vt2\times\rho2)/((\mathrm{dBz1}-\mathrm{dBz2})\times\rho)$, in which *qr*1, *vt*1, ρ1, dBz1 and *qr*2, *vt*2, ρ2, dBz2 indicate rain water, dropping speed, atmospheric density and radar reflectivity in the upper and lower levels, respectively.

$qc= -ir/(0.002\times qr^{0.875})$, in which *qr* is the rain water in the calculated level.

The adjustment of humidity field significantly improves the precipitation forecast of the model, including a scheme for moisture advection[18]. Therefore, the adjustment of humidity field is very important. In previous studies, the atmosphere where there exists radar echo is close to saturation and the relative humidity is set at 0.95 or the specific humidity is calculated as atmospheric saturated specific humidity. However, the method does not agree with the observation. In the actual observation, when there is precipitation in the ground, the relative humidity in the precipitation area is not 100% in most cases[19]. Therefore, it is not accurate that the specific humidity is calculated as the atmospheric saturated specific humidity. Generally speaking, the atmosphere is basically saturated when there exists cloud water (namely, $qc>0$), but *qc* cannot be directly calculated using the radar reflectivity. Consequently, the atmospheric saturated state is judged by *qr* which is directly calculated from the radar reflectivity, and then, the specific humidity is adjusted. The method is

presented in detail as follows. Eight grids around the calculated grid are chosen. When the *qr* value of the calculated grid is greater than zero and the *qr* values of five out of the eight grids are greater than zero, the specific humidity of the calculated grid is set as the saturated specific humidity and those of other grids are set at the specific humidity of the background field.

3 ANALYSIS OF THE NUMERICAL EXPERIMENT RESULTS

3.1 *Design of the experiments*

The GRAPES mesoscale numerical model is used, with a horizontal resolution of $0.03^{\circ}\times0.03^{\circ}$ and 31 vertical levels. The forecast region of the model ranges from 109°E to 118.24°E and from 19°N to 26.98°N, and the number of the grids is 309×267. The height of the model top is about 28 kilometers and the time integrating step is 90 seconds. The physical schemes include KFETA cumulus cloud convective parameterized scheme, cloud microphysical WSM6 scheme (WRF Single-Moment 6-class) with the mixing phase such as cloud water, rain water, ice-snow, graupel, MRF boundary layer scheme, slab land surface scheme and a rapid radiative transfer model (RRTM) long-wave radiation. The four schemes are designed, including (1) control experiment (Ctrl), with the cloud water (*qc*), rain water (*qr*) and specific humidity (*qv*) unchanged in the initial field of model, (2) experiment one (Exp. 1), with *qc* and *qr* adjusted by using the nudging method in the initial field of model, (3) experiment two (Exp. 2), set as in Exp. 1, but also with *qv* adjusted by using nudging method in the initial field of model and with *qv* taken from the background field, and (4) experiment three (Exp. 3), set as in Exp. 2, but first with *qv* adjusted according to *qr*.

The nudging method mentioned above indicates that a linear forcing term is added to the predictive equation during the period of simulating δ*t* in model integration and the term is a ratio to the difference between the forecast and observation, which aims at making the model forecast close to the observation.

$$w^t = w_m^t + \alpha \times (w_0^t - w_m^t)$$

In the formula, α is the ratio between the time step d*t* of the model and the time period δ*t* of the simulation; $w_m{}^t$ is the forecast value of the model integrated at the *t*-th step and $w_o{}^t$ is the observed value (or the retrieved value) at the same time; w^t is the *t*-th forecast value after the nudging adjustment. δ*t* is 1080 s, or, 12 integrating steps (an empirical value). The simulated period begins at 08:00 on May 14 and ends at 08:18 on May 14.

The integration of the model starts at 08:00 on May 14 and lasts for 12 hours. The output of the model is given hourly and the forecast of NCEP with 1°×1° is given as the lateral boundary condition, available every six hours.

3.2 *Analysis of the results*

3.2.1 DISTRIBUTION OF RADAR REFLECTIVITY, RAIN WATER AND VAPOR IN THE INITIAL FIELD

The distribution of radar reflectivity, a *qr* calculated by radar reflectivity, an unrevised *qv* and a revised *qv* at the 3-km height are given in Fig. 2, with the horizontal resolution of radar reflectivity at 1 km and that of *qr* and *qv* at 3 km. The distribution of *qr* (Fig. 2b) is similar to that of radar reflectivity (Fig. 2a) and the main rainband of precipitation (Fig. 1a). In other words, there exists a zonal distribution from Fujian, Jiangxi, southern Hunan, northern Guangdong to central Guangxi. Therefore, the calculated *qr* is reasonable and can generally reflect the true condition of radar reflectivity. Comparing with the unrevised *qv* and the revised one (Fig. 2c and 2d), the water vapor increases in southern Fujian, western Hunan, northern Guangdong and central Guangxi after *qv* is revised. The distribution of revised water vapor is very similar to that of the rainband, radar reflectivity and *qr*, which indicates the adjusted *qv* can well reflect the true condition of the atmosphere.

3.2.2 COMPARISON OF THE RESULTS OF SIMULATED RADAR REFLECTIVITY

The simulated radar reflectivity in the four experiments and the observed radar reflectivity at 09:00 are given in Fig. 3. From the Ctrl (Fig. 3a), the simulated radar reflectivity only appears in the junction between Hunan and Guangxi as well as in the middle of Guangxi and part of Fujian. It is specially noted that the radar reflectivity in northern Guangdong is not simulated. The other three experiments (Fig. 3b, 3c and 3d) can simulate the zonal radar reflectivity from Fujian, Jiangxi, southern Hunan as well as northern Guangdong and Guangxi, which is similar to the observation (Fig. 3d). The intensity of simulated radar reflectivity in Exp. 3 and Exp. 4 is stronger than that in Exp. 2, especially in the Exp. 4, in which it is much stronger in northern Guangdong and the distribution of simulated radar reflectivity in the middle of Guangxi is very close to the observation. Though the intensity of simulated radar reflectivity is weaker than the observation, the simulated radar reflectivity in Exp. 2, Exp. 3, and Exp. 4 is close to the observation, which shows that the forecast of radar reflectivity is improved because of the adjusted humidity field. Simultaneously, the simulated and observed radar reflectivity at 10:00 and 11:00 are analyzed (figure omitted) and the results are generally similar to the forecast for the first hour.

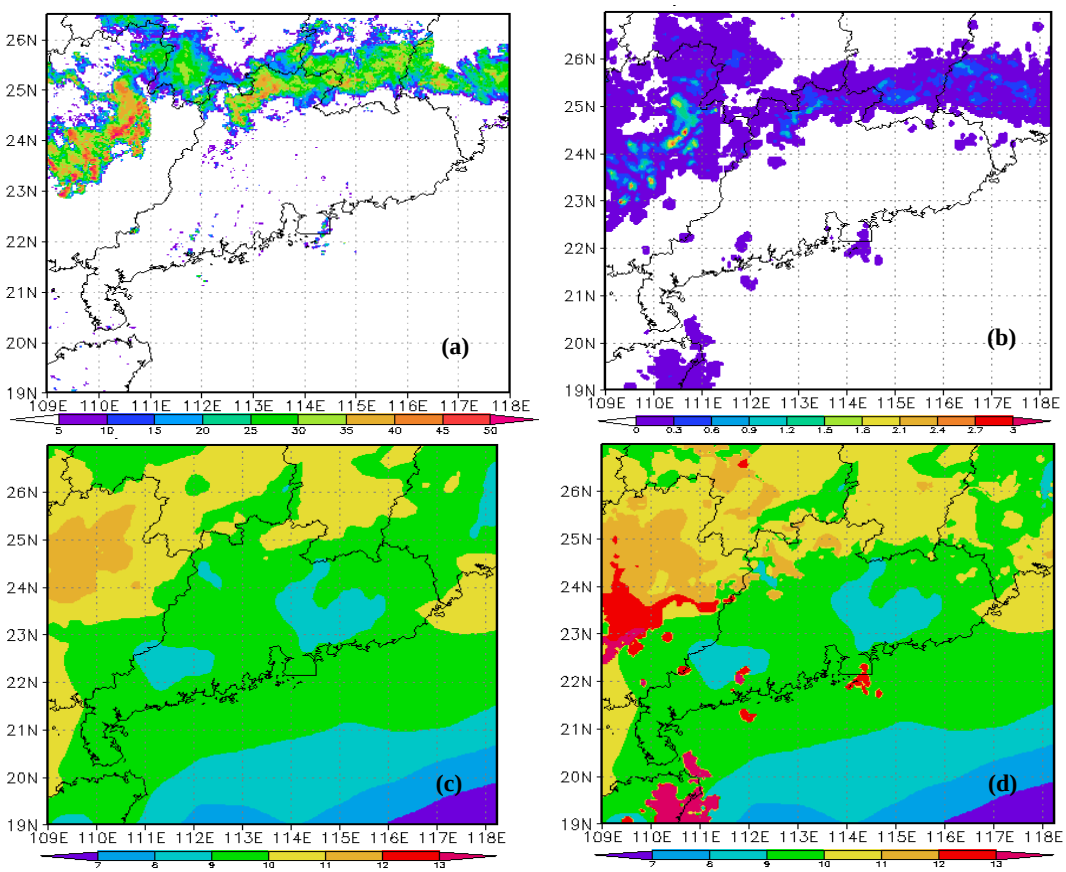

Figure 2. Radar reflectivity at 3 km (a, unit: dBz), *qr* (b, unit: g/kg), unrevised *qv* (c) and revised *qv* (d, unit: g/kg).

From the simulated radar reflectivity for the first three hours, it is known that the simulated results of Exp. 1, Exp. 2, and Exp. 3 are better than those of the Ctrl and the distribution and intensity of the simulated radar reflectivity in Exp. 2 and Exp. 3 are closer to the observation than Exp. 1. In particular, the radar reflectivity in northern Guangdong and middle-eastern Guangxi is simulated only in Exp. 3. However, the distribution of radar reflectivity from Fujian, Jiangxi, southern Hunan as well as northern Guangdong and Guangxi are shown in Exp. 1, Exp. 2, and Exp. 3. Consequently, the differences of the simulated results of 0–3 h nowcasting in the three experiments are not obvious and the results of 4–6 h forecast are analyzed.

From the simulated radar reflectivity of the four experiments at the fourth hour, namely, at 12:00 (Fig. 4), the simulated results in Exp. 1 (Fig. 4a) and Ctrl (Fig. 4b) are similar and neither can simulate the zonal distribution of radar reflectivity. The zonal distribution of radar reflectivity similar to the observation is simulated in Exp. 2 (Fig. 4c) and Exp. 3 (Fig. 4d). However, the location is more northward and the intensity is weaker. Comparing the simulated results between Exp. 2 and Exp. 3 reveals that the simulated radar reflectivity is consistent in Exp. 3, especially, the radar reflectivity in middle-eastern Guangxi is simulated in Exp. 3 and its intensity is close to the observation than in Exp. 2. There are obvious differences in the simulated radar reflectivity between the fifth and sixth hour in the four experiments. In Exp. 1 and Ctrl, similar to the fourth simulation, only the radar reflectivity at the conjunction of Guangxi, Guangdong and Hunan is simulated and the radar reflectivity in other areas cannot be simulated. In Exp. 2 and Exp. 3, the difference of the simulated radar reflectivity is larger than in the simulation for the fourth hour and the difference is more obvious when the prediction time is much longer. The maximum difference of the simulated radar reflectivity appears in the conjunction between southern Jiangxi and Guangdong. The simulated radar reflectivity continues to weaken at the fifth and sixth hour and the simulated radar reflectivity in Fujian and Guangdong as well as Guangxi has a break in Exp. 2. In Exp. 3, the simulated radar reflectivity in southern Jiangxi weakens, but the zonal radar reflectivity at the fifth and sixth hour can be well simulated from Fujian, southern Jiangxi, northern Guangdong to Guangxi. From the latter three values of simulated radar reflectivity, it is known that the differences are much distinct in Exp. 2, Exp. 3 and Exp. 4. The simulated results in Exp. 3 and Exp. 4 are better than in Exp. 2, especially in Exp. 4, in which the forecast is much

improved.

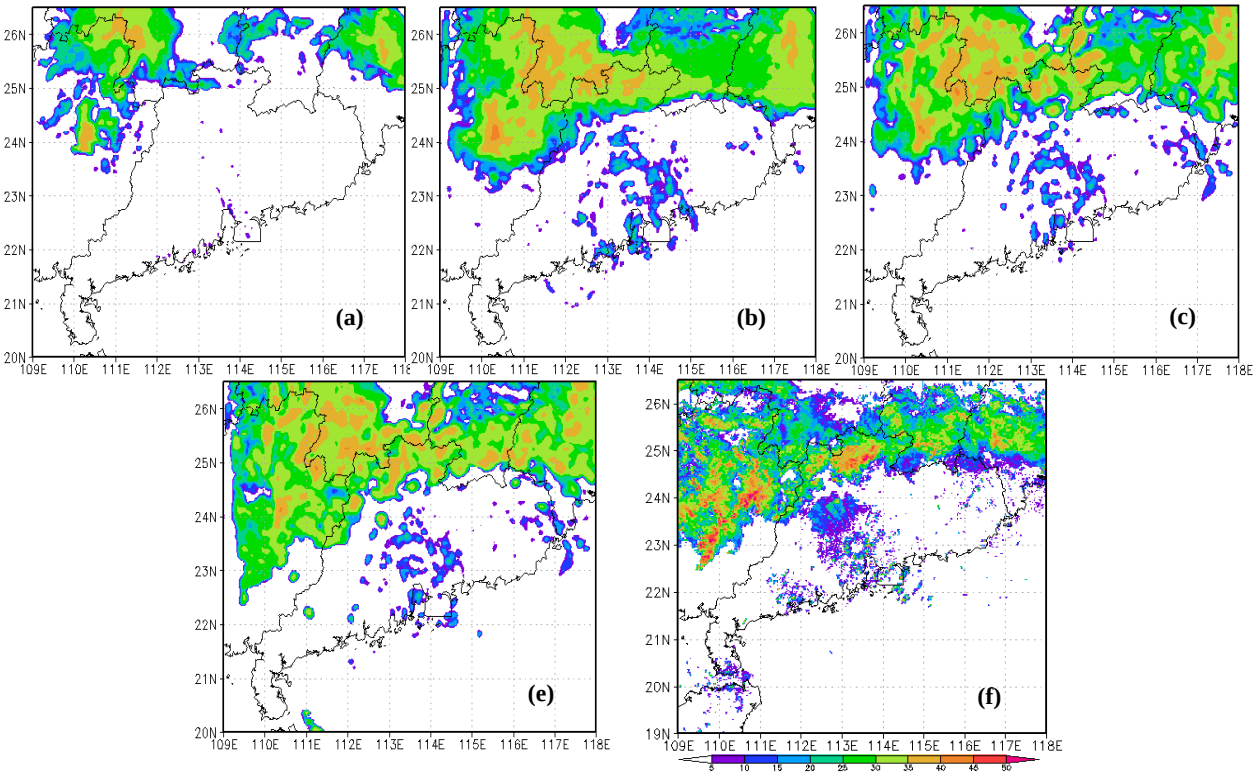

Figure 3. Model forecast radar reflectivity at the first hour in the four experiments and observation a. Ctrl; b. Exp.; 1 c. Exp. 2; d. Exp 3; e. Observation.

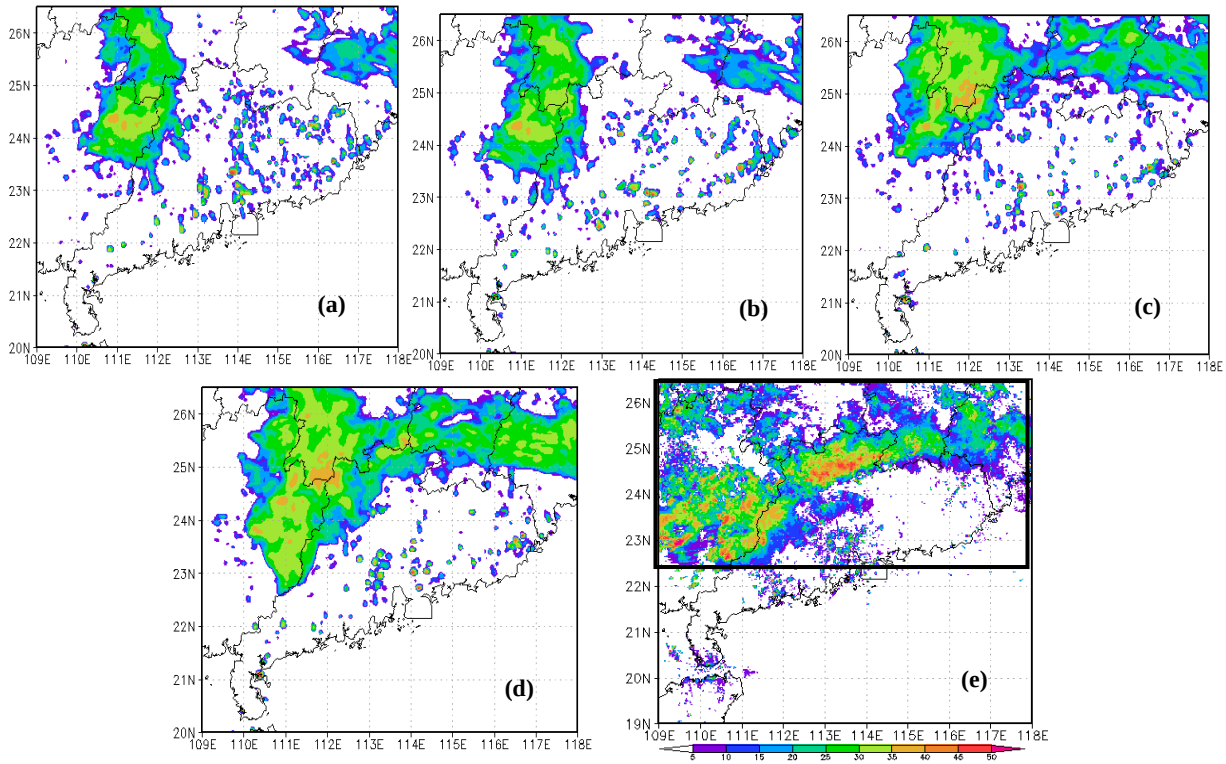

Figure 4. Same as Fig. 3 but for the radar reflectivity forecast at the fourth hour.

Comparing the nowcasting of the 0–6 h radar reflectivity from the four experiments with the observation shows that when *qc*, *qr* and *qv* are unadjusted in the initial field, the forecast 0–6 h radar reflectivity is weaker and its distribution is discontinued. When *qc* and *qr* are adjusted using the

nudging method in the initial field, the forecast 0–3 h radar reflectivity is much improved and the intensity and distribution are close to the observation, but the forecast 4–6 h radar reflectivity is similar to that of the Ctrl. When *qc*, *qr*, and *qv* are adjusted, the 0–6 h forecast is much improved, especially in Exp. 4 in which the radar reflectivity is simulated in the middle-eastern Guangxi and the distribution is continuous and the intensity is close to the observation in the 0–6 h forecast, which is better than in the other three experiments. Based on what is discussed above, the adjusted humidity through the calculated *qr* based on the radar reflectivity is reasonable and can improve the forecast 0–6 h radar reflectivity in the model.

From the above qualitative analysis, the 0–6 h nowcasting of radar reflectivity in the model is improved to a certain extent when *qv* is adjusted by the nudging method in the initial field. Consequently, the differences of the simulated radar reflectivity with or without the adjusted *qv* are quantitatively given based on the bias (BIAS), probability of detection (POD), and critical success index (CSI). The assessment range of radar reflectivity is from 109° to 118°E, 22.5° to 26.5°N (Fig. 4e). Firstly, the radar reflectivity data in the assessment region is interpolated into the data with a horizontal resolution of 0.03°×0.03°, which is the same as the horizontal resolution of the model. Secondly, the maximum composites of radar reflectivity for both the observation and simulation are estimated and the maximum radar reflectivity at some grids is derived from the maximum of the grids in vertical levels. The formulas of calculating the BIAS, POD and CIS are as follows:

$$\mathrm{BIAS}=\frac{1}{N_f}\sum_{i=1}^{N_f} f_i \,/\, (\frac{1}{N_o}\sum_{i=1}^{N_o} F_i)$$

in which N_j indicates the grid number when the forecast value is greater than zero, f_i is the forecast value, N_0 is the same as N_j but the observation and F_i are the observed values.

$$\mathrm{BPOD}=\frac{a}{a+b}, \qquad \mathrm{CSI}=\frac{a}{a+b+c}$$

Here, when the observation is equal to or greater than the threshold and the forecast is equal to or greater the threshold, the numbers of stations are marked with “a”. When the observation is less than the threshold and the forecast is equal to or greater than the threshold, the numbers of stations are marked with “b”. When the observation is equal to or greater than the threshold and the forecast is less than the threshold, the numbers of stations are marked with “c”.

In order to compare with the overall difference, the biases of the Ctrl, Exp. 1, and Exp. 3 are given (Figure omitted) and the biases fluctuate around the value of 1. The absolute biases of the three experiments are given in Fig. 5 and the result shows that the errors of Exp. 1 and Exp. 3 are greater than those of the Ctrl in the first three hours but less than that of the Ctrl in the 4th–6th hours. Therefore, the forecast is improved when the cloud parameters and humidity are adjusted in the initial field. Comparing Exp. 1 with Exp. 3 indicates that the forecast errors in the other hours in Exp. 3 are smaller than in Exp. 1 except for the second and third hour, especially the fourth to sixth hour, showing that the radar reflectivity forecast by the model is obviously improved because of the adjusted humidity.

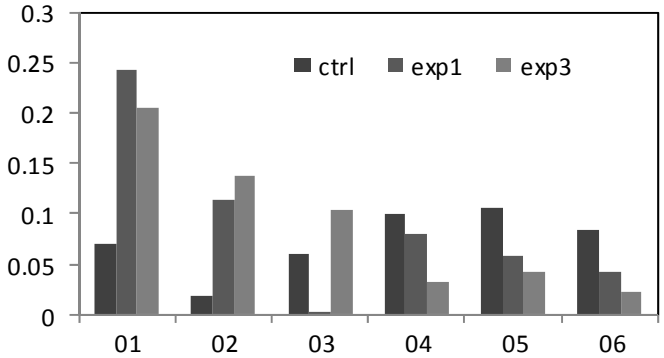

Figure 5. Variations of biases with time in the Ctrl, Exp. 1 and Exp. 3.

The radar reflectivity is divided into four grades, which are 5, 15, 25, 35 dBz, to assess POD and CSI respectively. The distributions of POD and CSI of the four grades changing over time in the Ctrl, Exp. 1 and Exp. 3 are given in Fig. 6 and the changing tendency is basically similar in the three experiments. With the extension of forecast duration, the POD and CSI are smaller and with the grades of radar reflectivity increasing, both are also smaller. Comparing POD with CSI in the three experiments shows that the results in Exp. 1 and Exp. 3 are better than in the Ctrl and with the radar reflectivity increasing, the difference is much more obvious. Comparing with the results between Exp. 1 and Exp. 3 finds that the

difference of radar reflectivity above 5 dBz is not obvious and for the 15, 25, 35 dBz, the POD and CSI in Exp. 3 are better than in Exp. 2, especially in the radar reflectivity above 25 dBz. The false prediction rates in the three experiments are given (Figure omitted) and the variation tendency is contrary to that of the POD and CSI, i.e., the FAR increases with the increase of forecast duration and the strengthening of radar reflectivity. From the discussion above, the POD and CSI increase and the FAR decreases after *qv* is adjusted by the nudging method, and particularly, the forecast effect of radar reflectivity above 25 dBz is well improved.

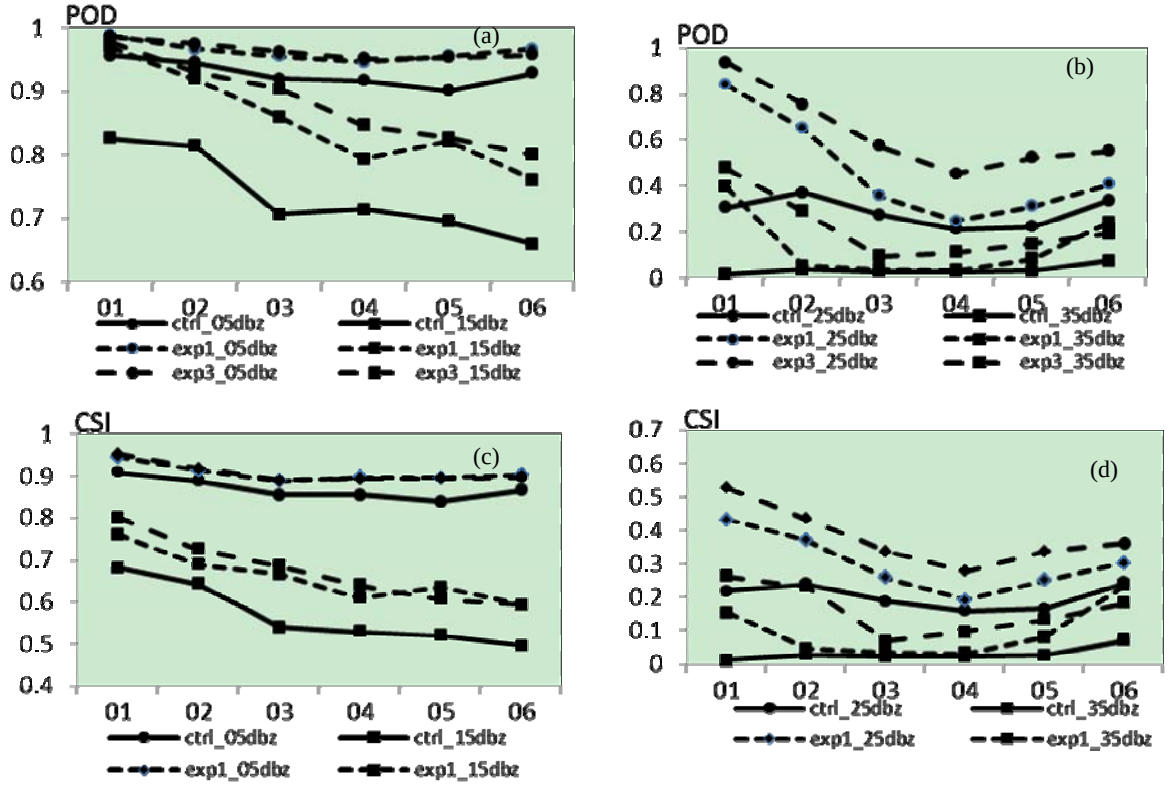

Figure 6. Distributions of POD (a, b) and CSI (c, d) of radar reflectivity at different ranks with time (solid line: Ctrl; dotted line: Exp. 1; dashed line: Exp. 3)

3.2.3 ANALYSIS OF SIMULATED PRECIPITATION

The precipitation distributions of 0–3 h forecast in all experiments are given as follows. The precipitation amount for the first-hour model forecast is given in Fig. 7 and the results in Exp. 1 (Fig. 7b), Exp. 2 (Fig. 7c), and Exp. 3 (Fig. 7d) are better than in the Ctrl (Fig. 7a). Comparisons between the observed and simulated precipitation show that the precipitation amount of the latter is weaker than that of the former. It also indicates that the distributions of simulated precipitation in Exp. 1, Exp. 2, and Exp. 3 are similar to the observation, especially Exp. 2 and Exp. 3. By contrast, the distribution of precipitation in Exp. 3 is a little better than in Exp. 2. The forecast effect of the first hour is well improved after *qv* is adjusted by the nudging method, especially, the forecast effect with adjusting *qv* which is revised by *qr* is a little better than of the unrevised *qv*.

Comparisons of the 1-h rainfall forecast between the forecasts of the second and the third hour in the four experiments (Figs. 8 & 9) show that the forecast effect on the second hour is similar to that of the first hour and the forecast in the three experiments is better than in the Ctrl. The amount and distribution in Exp. 2 and Exp. 3 are close to the observation (Fig. 1c). The difference of forecast at the third hour is large in the four experiments. The 1-h rainfall simulated in Exp. 1 is similar to that in the Ctrl and neither can simulate the precipitation centre and the rainfall amount is less than 5 mm in northern Guangdong. In Exp. 2, the rainfall amount greater than 5 mm in the 1-h rainfall simulation occurs in northern Guangdong, however, the precipitation range is small and the precipitation amount is little. In Exp. 3, both the precipitation range greater than 5 mm and the amount in northern Guangdong increase, which is much closer to the observation than in Exp. 2. The results for 4–6 h forecast in the four experiments are similar and much

different from the observation.

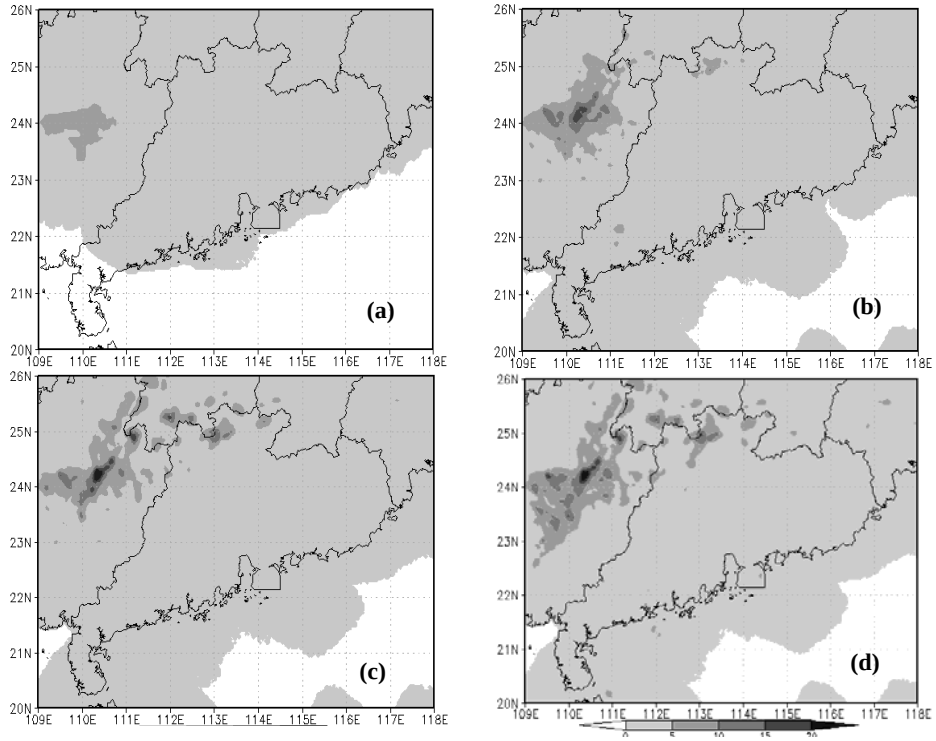

Figure 7. Model forecast precipitation at the first hour. Unit: mm . a: Ctrl; b. Exp. 1; c. Exp. 2; d. Exp. 3.

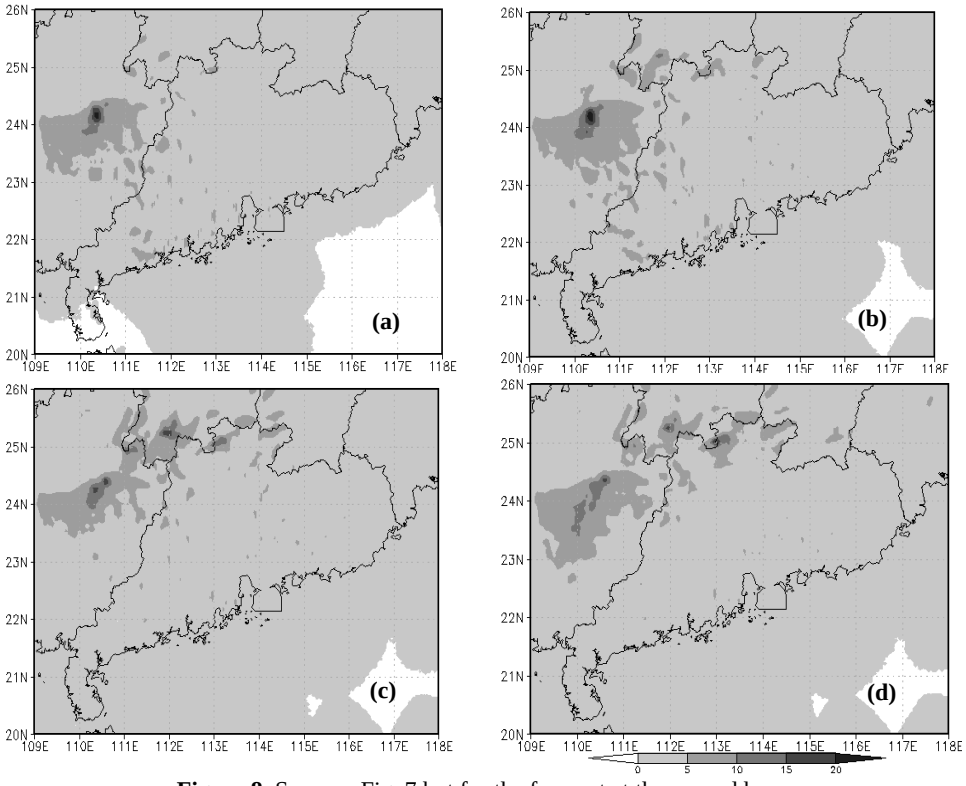

Figure 8. Same as Fig. 7 but for the forecast at the second hour.

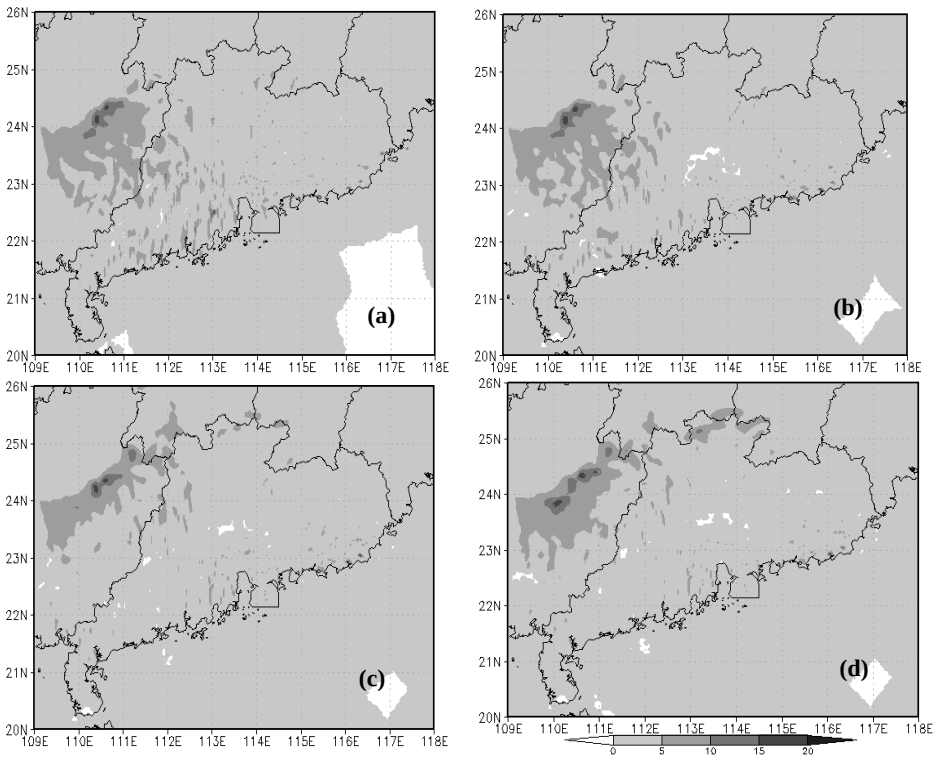

Figure 9. Same as Fig. 7 but for the precipitation forecast at the third hour.

From the simulated precipitation in the four experiments, in which *qc*, *qr* and *qv* are unadjusted in the initial field, the precipitation centre in northern Guangdong cannot be simulated during the 0–3 h forecast and the rainfall amount there is less than 5 mm. When *qc* and *qc* are adjusted with the nudging method, the rainfall amount greater than 5 mm occurs but the range and intensity are smaller and weaker in northern Guangdong during the 0–2 h forecast. For the forecast of the third hour, the result is the same as the Ctrl. When *qc*, *qr* and *qv* are adjusted with the nudging method, the region of rainfall amount greater than 5 mm expands and the intensity strengthens, especially, when *qv* retrieved by *qr* is adjusted, the region of rainfall amount greater than 5 mm in central Guangxi extends and the rainfall distribution in northern Guangdong is much closer to the observation. The simulated rainfall amount in the four experiments is less than in the observation.

3.2.4 Analysis of causes

It is known from what is mentioned above that when only *qc* and *qr* are adjusted or *qc*, *qr* and *qv* are all adjusted in the initial field of model, the nowcasting of radar reflectivity and precipitation are improved to a certain degree, but with different amplitude with increasing forecast duration. Therefore, the reasons are analyzed by comparing the vapor and stream fields in this section. According to the previous analysis, the forecast of the model with the initial field adjusted by *qv* revised is better than that before the adjustment. Therefore, different forecast fields are given in the analysis below with the initial field adjusted by the *qc* and *qr* only (Exp. 1) and with it adjusted by the *qc* and *qr* and with *qv* revised (Exp. 3). In order to explain the reasons of differences in different forecast duration in the two experiments, different fields are given and the level is chosen at 850 hPa.

The differences of vapor field from 0–3 h forecast of the model between Exp. 3 and Exp. 1 are given in Fig. 10 (a, b & c) and the positive distribution of vapor field appears from Fujian, Jiangxi, southern Hunan, northern Guangdong to middle Guangxi. The distribution of maximum vapor is similar to that of the 0–3 h simulated radar reflectivity and 1-h rainfall when the initial field of model is adjusted by *qv*. Furthermore, the distribution of maximum vapor is also similar to that of the initial vapor field where *qv* is adjusted. Therefore, when the humidity is adjusted in the initial field, the model forecast vapor is adjusted accordingly, which is in favor of improving precipitation forecast. The differences of vapor between Exp. 3 and Exp. 1 during the 4- to 6-h forecast (Figure omitted) are analyzed and there still exists a positive vapor distribution, but the difference decreases with increasing forecast duration. Consequently, with increasing forecast duration, the differences of the two experiments decrease through the model's own adjustment and adaptation, in which the differences of 0–3 h forecast are obvious, the differences of 4–6 h forecast decrease, and the differences after the 6th hour are not obvious.

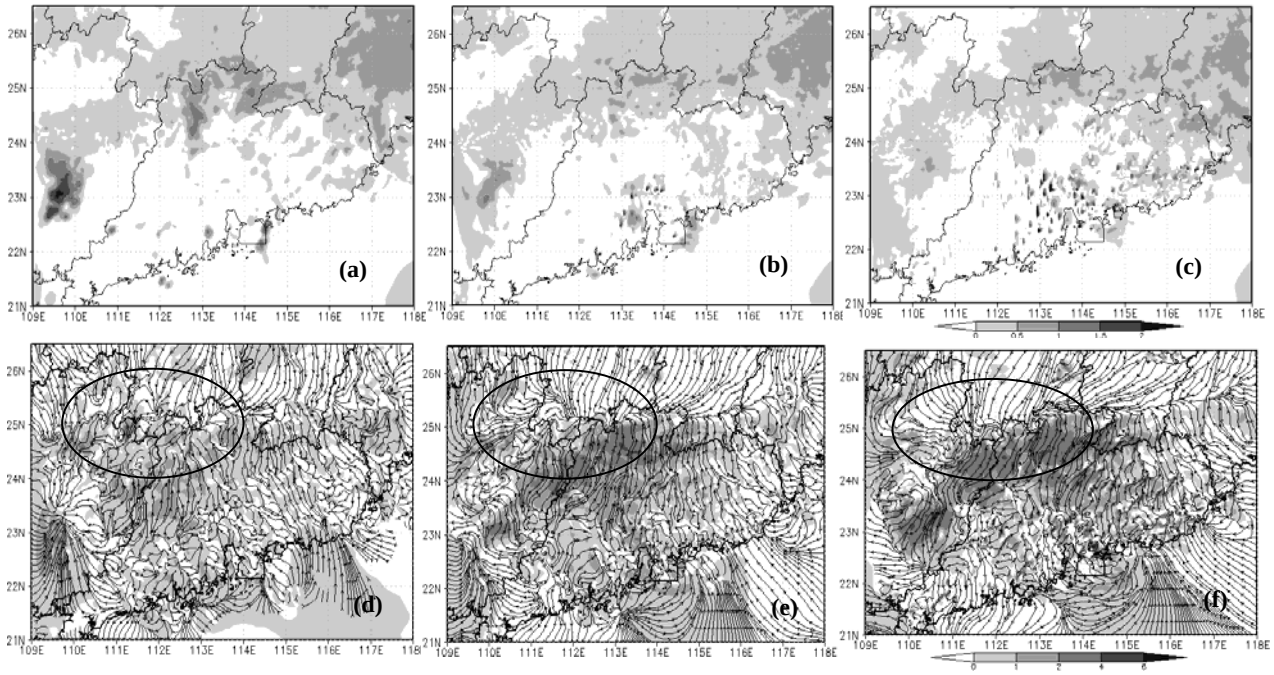

Figure 10. Model forecast difference fields at 850 hPa at the third hour between Exp. 3 and Exp. 2. a, b, c: vapor field (the shades are for areas greater than zero, unit: g/kg); d, e, f: stream field (the shades are for areas greater than zero, indicating the velocity).

When the vapor field is adjusted, the temperature, pressure and stream fields are also adjusted. As far as the stream field, the differences of 0–3 h forecast in the two experiments are given (Fig. 10 (d, e, & f)) and the convergence belt of differences field during the 0- to 3-h forecast occurs in northern Guangdong and middle Guangxi and the positive velocity region occurs in the southeast of the convergence belt. The reasons may be that the vapor increases in southern Jiangxi, northern Guangdong and all through to Guangxi after *qv* is adjusted, strengthening the warm and wet air from the southwest and cold air from the north and the stream field has to be adjusted. The precipitation process is mainly caused by troughs of low pressure and the cold air from the east route as well as the shear line moving toward the south (the shear of southwest and northeast wind). Therefore, the southwest and northeast wind strengthens to some extent. The differences of vapor transport and vapor flux divergence show that the vapor transport from the northwest increases and vapor convergence strengthens in northern Guangdong and Guangxi, which is favor of the precipitation increasing. In the two experiments, the difference decreases with the forecast duration increasing.

4 CONCLUSIONS AND DISCUSSION

(1) The radar reflectivity during the 0–3 h model forecast is significantly improved when *qc* and *qr* are adjusted by the nudging method in the initial field of model. The forecast of radar reflectivity after the third hour is close to that of the Ctrl. The forecast of precipitation in the first two hours is only slightly improved.

(2) The radar reflectivity during the 0–6 h model forecast is much improved when *qc, qr* and *qv* are adjusted by the nudging method in the initial field of model. The forecast in the first three hours is better than in the experiment with only cloud water and rain water adjusted and the distribution and intensity of radar reflectivity are much similar to the observation. The forecast of precipitation in the first three hours are improved.

(3) Comparing the humidity fields adjusted by the unrevised and revised *qv* by the nudging method shows that the forecast with adjusting the revised *qv* is better than that of adjusting the unrevised *qv*, especially in the 4–6 h forecast. The forecast of precipitation is also different, especially in the forecast after the third hour.

(4) Causes analysis. The vapor field is adjusted in the initial field of model, especially, the saturated vapor is considered, and the vapor field of model forecasting is accordingly adjusted, which adjusts the whole atmospheric condition and influences the forecast of radar reflectivity and precipitation.

In addition, the forecast results of the case initiating at 06:00 are analyzed and the conclusions are similar to those at 00:00, which indicates the vapor field adjusted in the initial field of model is basically reasonable. The nowcasting during 0–6 h is improved to some extent, but more cases need to be simulated to prove the results.

REFERENCES:

[1] SUN J, FLICHER D, LILLY D. Recovery of three-dimensional wind and temperature fields from single-Doppler radar data [J]. J. Atmos. Sci., 1991, 48(6): 876-890.
[2] LAROCHE S, ZAWADZKI I. A variational analysis method for retrieval of three-dimensional wind field from single Doppler radar data [J]. J. Atmos. Sci., 1994, 51(18): 2664-2682.
[3] LIU Li-ping. Experimental study of using double Doppler radar inversing three-dimensional wind field of precipitation system [J]. Quart. J. Appl. Meteor., 2003, 14(4): 502-506.
[4] ZHOU Hai-guang, ZHANG Pei-yuan. A new technique of recovering three-dimensional wind fields from simulated dual-doppler radar data in the Cartesian space [J]. Acta Meteor. Sinica, 2002, 60(5): 585-593.
[5] TANG Xi-ba, XUE Ji-shan. Preliminary study of the use of cosmic data in the global 3-dimensional variance assimilation system of grapes [J]. J. Trop. Meteor., 2009, 25(5): 521-531.
[6] QIU Chong-jian, YU Jin-xiang. Use of Doppler-radar data in improving short-term prediction of mesoscale weather [J]. Acta Meteor. Sinica, 2000, 58(2): 244-249.
[7] XU Jia-liang, MU Hai-zhen, Numerical simulation and analysis of offshore wind field features in Shanghai under the influence of typhoon [J]. J. Trop. Meteor., 2009, (3): 281-286 (in Chinese).
[8] GAO J D, COAUTHORS. Multiple Doppler wind analysis and assimilation via 3DVAR using Simulated observations of the Planned Case Network and WSR-88D radars [C]. 32nd Conf. Radar Meteor. Albuquerque, NM: Amer. Meteor. Soc., 2005.
[9] WOLLCOTT S W, WARNRE T T. A humidity initialization utilizing surface and satellite data [J]. Mon. Wea. Rev., 1981, 109(9): 1988- 989.
[10] HAASE G, CREWELL S, SIMMER C, ct al. Assimilation of radar data in mesoscale models: Physical initialization and latent heat nudging [J]. Phys. Chem. Earth, 2000, 25(12): 1237-1242.
[11] MILAN M, AMEN F, VENEMA V, et al. Physical initialization to incorporate radar precipitation data into a numerical weather prediction model (Local model) [R]. The 32nd Conference on Radar Meteorology, American Meteorological Society, Albuquerque, New Mexico, August 18 2005.
[12] ZHANG J. Moisture and diabatic initialization based on radar and satellite observations [D]. Norman, Oklahoma, 1999.
[13] TUO Ya, LIANG Hai-he, MA Shu-fen, et al. A preliminary research on improving MM5 initial fields using radar data [J]. J. Nanjing Inst. Meteor., 2003, 26(5): 661-664.
[14] WANG W, WARNER T T. Use of four-dimensional data assimilation by Newtonian relaxation and latent-heat forcing to improve a mesoscale-model precipitation forecast: A case study [J]. Mon. Wea. Rev., 1988, 116(12): 2593-2613.
[15] GUO Xia, DANG Qing-ren. The use of radar data in the numerical simulation of heavy rainfalls in the Changjiang-Huaihe Rivers basin [J]. J. Trop. Meteor., 1999, 15(4): 352-362.
[16] LI Yong-ping, YUAN Zhao-hong, WANG Xiao-feng. Microphysical adjustments using reflectivity of Doppler radar for mesoscale model [J]. Quar. J. Appl. Meteor., 2004, 15(6): 658-666.
[17] BREWSTER K. Application of a Bratserth analysis scheme including Doppler radar data [C]. 15th Conference on Weather Analysis and Forecasting, Amer. Meteor. Soc., Norfolk, 1996: 92-95.
[18] CHEN Zi-tong, WAN Qi-lin, SHEN Xun-shun, et al. Comparisons and improvement of water vapor advection schemes of grapes regional model [J]. J. Trop. Meteor., 2010, 26(1): 1-6.
[19] QIN Yan-yan, LI Bo, ZHANG Pei-yuan. A study of the relationship between radar reflectivity of rain and relative humidity of atmosphere [J]. Chin. J. Atmos. Sci., 2006, 30(2): 351-359.

Citation: ZHANG Yan-xia, CHEN Zi-tong, MENG Wei-guang et al. The influence of cloud parameterization adjustment using reflectivity of Doppler on nowcasting with GRAPES model. *J. Trop. Meteor.*, 2014, 20(2): 181-192.